Fuel 428 (2027) 140213

Contents lists available at ScienceDirect

Fuel

journal homepage: www.elsevier.com/locate/fuel

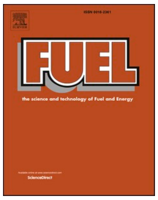

Full Length Article

A novel flame-stabilization strategy: Symmetric tesla-valve microchannel for microscale hydrogen combustion

Chenghua Zhang [a], Yunfei Yan [a,*], Yonghong Wu [a], Zikang Niu [a], Chang Liu [a], Wen Siang Lew [b,*]

[a] Key Laboratory of Low-grade Energy Utilization Technologies and Systems, Chongqing University, Ministry of Education, Chongqing 400030, China
[b] School of Physical and Mathematical Sciences, Nanyang Technological University, 21 Nanyang Link, Singapore 637371 Singapore

ARTICLE INFO

Keywords:
Micro combustion
Tesla-valve channel
Flame stability
Switching effect
Separation distance

ABSTRACT

Advances in microfabrication are driving micro-power systems, yet hydrogen-fueled micro combustors remain limited by combustion efficiency and flame stability at small scales. In this work, we numerically investigate a Tesla-valve microchannel (TMC) combustor that anchors the flame through cooperative main-tributary channel flows. Compared with a straight micro combustor (SMC), the TMC achieves higher combustion efficiency (98.09%) and a lower pressure drop (440.64 Pa) due to tributary channel induced flow blocking, producing a stable trident-shaped flame. Over a wide inlet velocity range of 2–42 m/s, a flow-switching transition occurs at 22–24 m/s, accompanied by sharp reductions in efficiency (93.23%→30.16%) and pressure drop (3,233.24 Pa → 1,160.92 Pa). This transition coincides with main channel flame detachment, confirming the velocity dependence of main-tributary flow partitioning. Systematic variation of the Tesla-valve island separation distance reveals the underlying mechanisms: small separations ($d = 1.2$ and 1.6 mm) strengthen tributary blocking and shear, enhancing efficiency and flame anchoring; intermediate separations ($d = 2.0$ and 2.4 mm) weaken blocking, promote flame opening, and trigger concurrent switching in efficiency and pressure; while a large separation ($d = 2.8$ mm) induces mild recirculation via expansion–contraction effects, enabling wall-attached combustion and partial efficiency recovery at high velocities. These results highlight the trade-off between flame stabilization and pressure-drop penalty, providing geometry-specific numerical insights for the further optimization of Tesla-valve micro combustors under different operating constraints.

1. Introduction

Recent advances in microfabrication have unlocked unprecedented opportunities for micro power systems [1]. However, conventional electrochemical batteries remain fundamentally constrained by limited energy density and unfavorable mass-to-volume ratios. Hydrogen, by contrast, offers a high heating value and intrinsic environmental advantages [2], positioning hydrogen-fueled micro combustors as promising candidates for delivering high-power-density, stable energy in micro energy systems [3]. Despite this potential, micro combustors with centimeter to millimeter-scale dimensions suffer from large specific surface areas that induce severe heat losses [4]. At the same time, increasing inlet velocities shorten hydrogen residence times, intensifying flame instability and blowoff. Together, these effects critically limit operational stability and efficiency in practical micro power applications [5]. Consequently, achieving high-efficiency hydrogen combustion with robust flame stability at the microscale remains a central and unresolved challenge in the field.

Extensive efforts have been devoted to enhancing combustion performance at the microscale. One prominent strategy involves fully or partially filling microchannels with porous media, which increases flow resistance to reduce gas velocity and extend residence time, while simultaneously enabling heat recirculation and fuel preheating through solid–fluid heat transfer [6]. The thermophysical properties of the porous insert strongly influence combustion behavior; in particular, high thermal conductivity media can efficiently transport heat from high temperature reaction zones toward the inlet, thereby preheating the incoming fuel and substantially improving combustion characteristics and overall efficiency [7].

Catalytic combustion represents another widely adopted approach for flame stabilization in micro combustors [8]. By coating channel walls with noble-metal catalysts, *e.g.*, Pt, Pd, Rh, surface active sites lower the

---

* Corresponding authors.
E-mail addresses: yunfeiyan@cqu.edu.cn (Y. Yan), wensiang@ntu.edu.sg (W.S. Lew).

https://doi.org/10.1016/j.fuel.2026.140213
Received 6 February 2026; Received in revised form 14 May 2026; Accepted 2 June 2026

apparent activation energy, allowing combustion to occur at lower temperatures and shorter residence times, thus enhancing flame stability [9]. Nevertheless, prolonged exposure to high temperatures can induce local overheating and catalyst deactivation, while the high cost of noble metals remains a major barrier to large-scale implementation [10].

Consequently, increasing attention has shifted toward structural optimization as a catalyst-free pathway to improve flame stability and combustion efficiency in micro combustors. Along this line, Lv *et al.* [11] designed a microchannel incorporating exhaust-gas recirculation (EGR) based on second-law analysis, demonstrating that recirculation markedly enhances combustion performance. Rong *et al.* [7] proposed a dual-channel counterflow combustor in which vertical structures intensify heat transfer and improve exergy efficiency, achieving higher combustion efficiency with reduced pollutant emissions. Building on this concept, Wu *et al.* [12] introduced rectangular inter-channel perforations, significantly improving outer-wall temperature uniformity and further enhancing overall energy-conversion efficiency.

Additionally, the introduction of a sudden-expansion geometry, such as a backward-facing step, generates a downstream recirculation zone and an associated shear layer. As demonstrated by Xu *et al.* [13], the recirculation of hot products and reactive radicals, together with enhanced shear-layer mixing and prolonged residence time, provides effective thermal and chemical feedback that improves combustion efficiency and stabilizes the flame. Incorporating a downstream converging section transforms the single sudden expansion into a closed cavity; compared with an open expansion, this configuration produces a stronger recirculation zone and a more robust flame-anchoring site, thereby intensifying thermal and radical feedback as well as mixing [14,15]. Consequently, the blow-off limit is increased and the flame stability range is broadened. The cavity size and geometry play a critical role in determining micro combustor performance. Peng *et al.* [16] showed that cavity dimensions significantly influence thermal characteristics and flame location, with a pronounced impact on flame stabilization. Xu *et al.* [17] further reported that increasing inlet velocity drives the main channel flame progressively downstream until blow-off occurs, typically accompanied by flame opening and fuel leakage. To mitigate this behavior, bluff-body stabilization strategies have been proposed, in which the incoming flow is forced around a bluff body, *e.g.*, circular, triangular, or rectangular, forming a stable low-velocity recirculation zone in its wake [18]. This zone continuously entrains fresh reactants while retaining high-temperature products and radicals, effectively acting as a pilot flame that enhances mixing and thermal/radical feedback, thereby improving flame stability and increasing the blow-off limit.

However, at high inlet velocities, the pilot flame is strongly compressed, weakening its stabilizing effect. To address this limitation, Zhang *et al.* [19,20] introduced a slotted bluff body that guides a fraction of the fuel into the low-velocity wake, significantly enhancing flame stabilization. Subsequent studies revealed that flow blockage and partitioning between the central and side streams are critical parameters; by incorporating baffles, Zhang *et al.* [21] tuned the blockage and optimized the center-to-side flow ratio to sustain stable combustion over a wider velocity range. Nevertheless, configurations relying solely on center-slotted bluff bodies often induce excessive shear in the side streams and insufficient mutual blocking between the center and side flows, ultimately constraining further improvements in stability. These limitations underscore the need for simple structural designs that exploit multi-stream interactions within microchannels to achieve superior combustion performance and robust flame stabilization.

Since Nikola Tesla first proposed the Tesla-valve, the concept has attracted broad interdisciplinary interest, particularly in flow manipulation and passive control [22,23]. Modern Tesla valves are generally classified as symmetric or asymmetric configurations composed of main and tributary channels. By orchestrating flow diversion, confluence, and jet impingement within the valve geometry, they induce recirculation, modulate momentum transfer, and achieve passive flow rectification without moving parts [24]. Owing to their purely structural design, Tesla valves offer simplicity, high reliability, and long service life, and have demonstrated considerable potential in fluidic control, heat-transfer enhancement, and combustion-related applications [25].

Hu et al. [26] investigated Tesla-valve flow behavior in building ventilation and showed that, compared with forward flow, reverse flow exhibits a substantially larger pressure drop due to pronounced lateral blocking of the main channel flow by tributary branches, resulting in overall velocity attenuation. Consistently, Huang et al. [27] reported strong flow separation and jet impingement during diversion and confluence, where kinetic energy is dissipated into vorticity, leading to reduced velocity and pressure. Building on these characteristics, Soltani et al. [28] applied Tesla valves to fuel-cell cooling and achieved a 15% enhancement in nanofluid heat-transfer coefficient under reverse-flow conditions, together with improved temperature uniformity. Zhao et al. [29–31] further developed Tesla-valve based planar micro combustors, demonstrating that valve orientation and geometry enhance convective heat transfer, thereby improving combustion efficiency and wall-temperature uniformity. Moreover, leveraging its unidirectional flow behavior, the Tesla valve has been explored as a flame-arresting element; Shen et al. [32] demonstrated its effectiveness in limiting flame propagation. Nevertheless, despite their demonstrated capability in passive flow regulation, Tesla valves have rarely been exploited for microscale combustion control. In particular, their role in flame anchoring and stabilization, and the coupled evolution of flow partitioning, flame structure, and combustion performance, remain largely unexplored, limiting rational design for micro combustor applications.

This study develops a symmetric Tesla-valve microchannel in which a tributary channel supplies a fraction of the fuel to sustain stable combustion, while its confluence with the main channel flow provides effective flame anchoring. We quantify the contribution of the tributary channel to combustion enhancement and flame stabilization, and then extend the operating velocity range to analyze the inlet-velocity dependence of main/tributary flow partitioning and the associated switching behavior. Finally, by varying the Tesla-valve island separation distance to regulate flow partitioning, we examine flame stability and operational robustness across different geometries. These findings provide numerical insight into flow-partitioning-assisted flame stabilization in the present Tesla-valve microchannel geometry.

2. Numerical model

2.1. Physical model

Fig. 1 illustrates the geometry of the Tesla-valve microchannel combustor (TMC) and straight-microchannel combustor (SMC). To isolate the contribution of the Tesla-valve tributary channels, the SMC consists only of a straight main channel identical in size to that of the TMC (no tributary channels). In the TMC, a pair of symmetric tributary channels branches from the main channel, with a width of $a = 2$ mm, at $L_1 = 4$ mm downstream of the inlet. Each channel has a length $L_2 = 5$ mm and departs at a diversion angle $\theta = 30^\circ$, the channel then flows into the main channel through a circular channel of radius $R = 2.5$ mm, forming a Tesla-valve flow path. The channel width is $c = 1$ mm, and all channels share a uniform height $b = 1$ mm, and the combustor body has an overall length $L = 20$ mm and width $W = 10$ mm. Quartz is selected to mitigate conductive heat loss and promote flame stabilization, with density, specific heat capacity, and thermal conductivity of 2,650 kg/m^3, 750 J/(kg·K), and 1.05 W/(m·K), respectively [33].

2.2. Mathematical model

The combustor has an overall size of 20 mm, even the smallest local hydrodynamic length scale is taken as the tributary channel width, $l = 1$ mm, which is much larger than the molecular mean free path λ. The

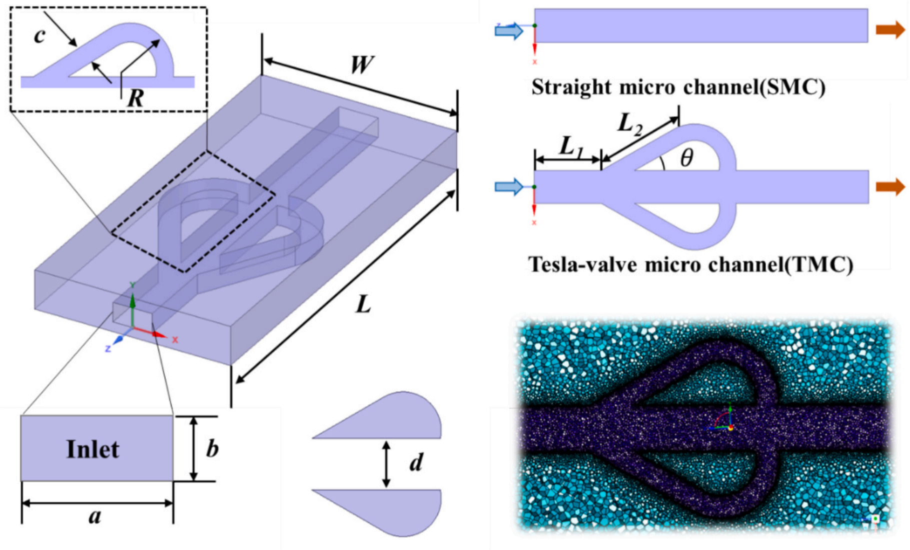

Fig. 1. Schematic diagram of Tesla-valve micro combustor.

resulting Knudsen number satisfies $K_n = \lambda / L < 10^{-3}$ under the operating conditions, hence the flow can be treated as a continuum and rarefaction effects are negligible[34]. The Knudsen number and the mean free path are evaluated as:

$$K_n = \lambda / L \tag{1}$$

$$\lambda = \frac{k_B T}{\sqrt{2} d^2 n P} \tag{2}$$

where k_B is the Boltzmann constant, T is the temperature, d is the molecular (collision) diameter, P is the static pressure, and n is the number density.

Due to the strong coupling among flow, heat transfer, and chemistry, the Tesla-valve micro combustor features pronounced flow diversion and confluence. Following the microscale criterion suggested by Kuo and Ronney [35], a turbulence closure becomes appropriate when the Reynolds number exceeds 500. In the present Tesla-valve microchannel, the diversion, confluence, local acceleration, shear-layer interaction, and recirculation induced by the valve geometry can increase the local velocity and, consequently, the local Reynolds number beyond this threshold. Therefore, the realizable $k - \varepsilon$ turbulence model is employed to capture the complex separated and recirculating flow features.

$$\frac{\partial(\rho k)}{\partial t} + \nabla \bullet (\rho k \vec{v}) = \nabla \bullet \left[\left(\mu + \frac{\mu_t}{\sigma_k}\right) \nabla k\right] + P_k + G_b - \rho\varepsilon - Y_M \tag{3}$$

$$\frac{\partial(\rho\varepsilon)}{\partial t} + \nabla \bullet (\rho\varepsilon \vec{v}) = \nabla \bullet \left[\left(\mu + \frac{\mu_t}{\sigma_\varepsilon}\right) \nabla \varepsilon\right] + \rho C_1 S\varepsilon - \rho C_2 \frac{\varepsilon^2}{k + \sqrt{\nu\varepsilon}} + C_{1\varepsilon} \frac{\varepsilon}{K} C_{3\varepsilon} G_b \tag{4}$$

where P_k is the production of turbulent kinetic energy, G_b denotes the buoyancy production term and Y_M the compressibility dissipation correction. σ_k and σ_ε are the turbulent Prandtl numbers for k and ε, respectively. Besides, C_1, C_2, $C_{1\varepsilon}$, and $C_{3\varepsilon}$ are the constants in the equations.

The governing equations are below [36]:

Continuity equation:

$$\frac{\partial \rho}{\partial t} + \nabla(\rho \vec{v}) = 0 \tag{5}$$

Momentum equations:

$$\frac{\partial(\rho \vec{v})}{\partial t} + \rho(\vec{v} \bullet \nabla \vec{v}) = -\nabla p + \nabla \bullet \left(\mu\left[\nabla \vec{v} + (\nabla \vec{v})^T - \frac{2}{3} \nabla \bullet \vec{v} I\right]\right) \tag{6}$$

Energy equation for fluid region:

$$\frac{\partial(\rho E)}{\partial t} + \nabla \bullet \vec{v}(\rho E + p) = \nabla \bullet \left[\lambda_f \nabla T + \sum_i h_i \rho D_{i,m} \nabla Y_i + \vec{v} \bullet \left(\mu\left[\nabla \vec{v} + (\nabla \vec{v})^T - \frac{2}{3} \nabla \bullet \vec{v} I\right]\right)\right] + S_h \tag{7}$$

Energy equation for solid region:

$$\frac{\partial}{\partial t}(\rho_s C_s T) + \nabla \bullet (\lambda_s \nabla T) = 0 \tag{8}$$

Species transport equation:

$$\frac{\partial \rho Y_i}{\partial t} + \nabla \bullet (\rho \vec{v} \nabla Y_i) = \nabla \bullet (\rho D_{i,m} \nabla Y_i) + R_i \tag{9}$$

In equation (5)–(9), ρ and $\vec{v}$ are the gas density and velocity vector, p, μ, I are the pressure, dynamic viscosity, identity tensor. E and T denote the total specific energy and temperature, λ_f and λ_s are the thermal conductivities of the fluid and solid. ρ_s and C_s are the solid density and specific heat, Y_i is the mass fraction of species i. $D_{i,m}$, h_i,R_i are the mixture-averaged diffusion coefficient, specific enthalpy, net production rate.

To calculate the hydrogen combustion, a detailed hydrogen oxidation mechanism involving 13 species and 19 elementary reactions was adopted [37]. For the boundary conditions, a velocity inlet and a pressure outlet were adopted, and heat exchange between the outer combustor wall and the ambient is considered as mixed convection–radiation, which can be calculated according to the following equation [38]:

$$q = h_0 (T_{w,o} - T_\infty) + \varepsilon\sigma(T_{w,o}^4 - T_\infty^4) \tag{10}$$

where $T_{w,o}$ and T_∞ denote the outer wall and ambient temperatures, h_0 is the external convective heat-transfer coefficient, 20 W/(m^2·K). ε is the wall emissivity, 0.85, and σ is the Stefan–Boltzmann constant, 5.67×10^{-8} W/(m^2·K^4).

2.3. Grid independence validation

Mesh resolution usually affects the numerical prediction, and mesh refinement reduces discretization error but increases computational cost. To resolve the Tesla-valve features, we adopted four refined meshes by prescribing a global maximum element size and a local size in the Tesla-valve main/tributary channels: (0.60, 0.09) mm, (0.50, 0.08) mm, (0.40, 0.07) mm, and (0.30, 0.06) mm, corresponding to 260,618 cells, 444,940 cells, 596,988 cells, and 888,777 cells. Fig. 2 compares the centerline temperature and centerline OH mass-fraction. According to centerline temperature and OH mass-fraction in Fig. 2**a** and Fig. 2**b**, the coarsest mesh exhibits noticeable deviations, particularly upstream whereas the curves collapse with refinement. Relative to the finest mesh (888,777 cells), the maximum deviations for the 596,988 cells mesh are only 1.46% (Centerline temperature) and 0.86% (Centerline OH mass fraction). Consequently, the 596,988 cells mesh is adopted for subsequent simulations as a balanced choice between accuracy and cost.

2.4. Model validation

To verify the reliability of the present numerical model, two complementary validation cases were conducted, as shown in Fig. 3. First, the wall-temperature distribution of a planar micro combustor was compared with experimental data [39]. The maximum and average errors were 5.15% and 3.10%, respectively, indicating that the combustion and heat-transfer model can reasonably predict the wall-temperature characteristics. Second, the pressure loss of a GMF Tesla valve was validated [25], where the maximum and average errors were 7.81% and 4.25%, respectively, confirming that the present model can predict the flow characteristics of the Tesla-valve channel. In addition, the numerical model adopted in this paper has been verified in the previous work [19–21], which also confirms the feasibility of the relevant numerical model. Therefore, the present numerical model is considered suitable for the subsequent simulations.

2.5. Data reduction

In data reduction, the key evaluated quantities include combustion efficiency, pressure loss, and flame length. Among them, the combustion efficiency is defined as follows:

$$\eta = \frac{m_{H_2,in} - m_{H_2,out}}{m_{H_2,in}} \times 100\% \tag{11}$$

where $m_{H_2,in}$ and $m_{H_2,out}$ represent the mass fractions of hydrogen at the inlet and outlet.

$$\Delta P = P_{in} - P_{out} \tag{12}$$

where ΔP represents the pressure loss, corresponding respectively to the pressure difference between the inlet and outlet.

Furthermore, by measuring the range along the flow direction of the area in the main channel and the tributary channel where the OH mass fraction exceeds a certain value (0.005), the flame length can be evaluated:

$$EFL = MFL + TFL \tag{13}$$

In the formula, *EFL* represents the effective flame length, which is the sum of the main flame length(*MFL*) and the tributary flame length(*TFL*).

3. Results and discussion

3.1. Combustion and flow characteristics

To quantify the benefit of the Tesla-valve design, a straight micro combustor (SMC) with identical main channel dimensions was constructed as a baseline, and both structures were compared over an inlet-velocity range of 1–7 m/s (Fig. 4. As shown in Fig. 4**a**, the combustion efficiency exhibits a growing gap between the two configurations with increasing velocity, η=97.58% for the SMC versus 98.08% for the TMC at 7 m/s, an improvement of 0.50 percentage points, indicating more complete combustion in the Tesla-valve micro combustor. As shown in Fig. 4**b**, the centerline temperature peak in the TMC shifts upstream, placing the high-temperature zone closer to the inlet, whereas the SMC maintains higher temperatures further downstream, consistent with a high-temperature zone rearward shift. According to temperature contours in Fig. 4**c**, with increasing inlet velocity, the SMC high-temperature zone rapidly drifts toward the outlet, at 7 m/s it becomes noticeably tilted and displaced downstream, and the high-temperature zone detaches from the micro combustor at 8 m/s. In contrast, the TMC exhibits a markedly slower rearward shift, evidencing anchoring of the high-temperature zone by the Tesla-valve structure. In particular, starting at v = 5 m/s, the high-temperature zone in the TMC develops a necked-shape near the main–tributary channel confluence, which becomes more pronounced at 7 m/s. The converging tributary flow and local recirculation suppress the downstream tilting and recession of the main high-temperature zone, accounting for the upstream shift and improved combustion efficiency.

To further elucidate the combustion state, we analyzed the centerline

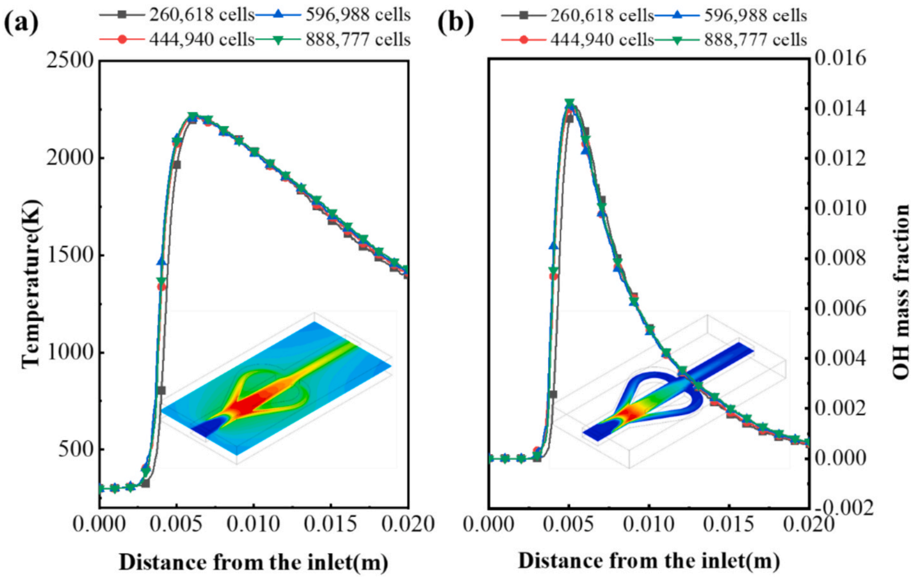

Fig. 2. Verification of grid independence: (a) Centerline temperature; (b) Centerline OH mass fraction.

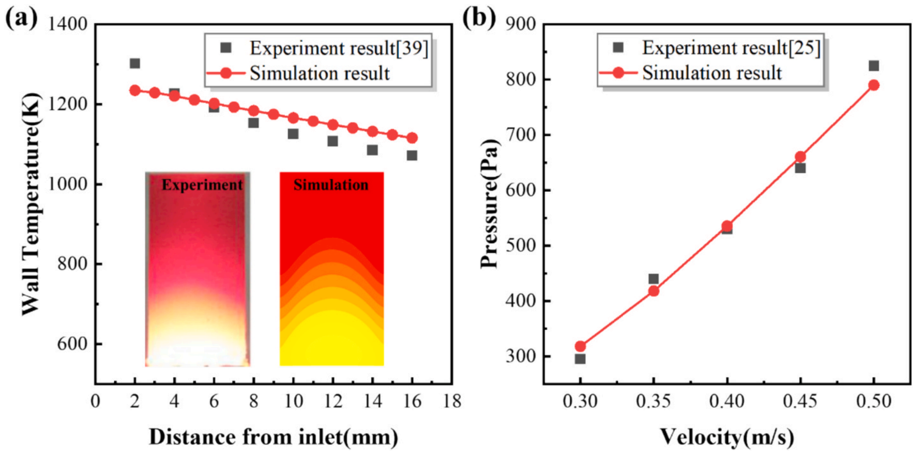

Fig. 3. Validation of the numerical model. (a) Comparison of simulated and experimental wall-temperature distributions in a planar micro-combustor. (b) Comparison of simulated and experimental pressure losses in a GMF Tesla valve.

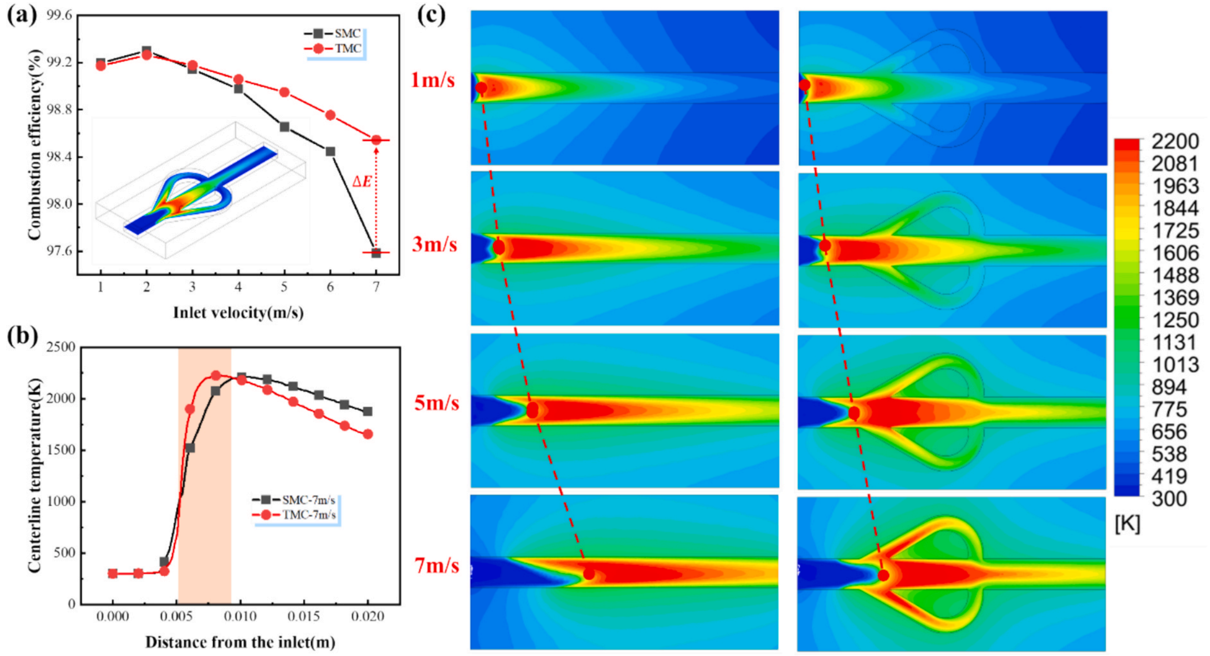

Fig. 4. Comparison between the Tesla-valve micro combustor (TMC) and the straight micro combustor (SMC): (a) Combustion efficiency versus inlet velocity; (b) Centerline temperature at 7 m/s; (c) Temperature contours at 1, 3, 5, and 7 m/s (SMC at left, TMC at right).

distributions of hydrogen (Y_{H_2}), OH radical (Y_{OH}), and the flame shape in the SMC and TMC. As shown in Fig. 5**a-b**, all cases exhibit a consistent crossover between Y_{H_2} and Y_{OH} near the reaction zone, Y_{H_2} decreases while Y_{OH} increases and then decays, indicating the conversion of hydrogen into OH during reaction progress. At low inlet velocities (1–3 m/s), the centerline hydrogen and OH radical for SMC and TMC nearly coincide, suggesting that under weak convection/long residence time the channel benefit of the Tesla-valve is not yet pronounced. When the velocity increases to 5 and 7 m/s, the SMC peaks shift downstream, whereas those in the TMC move upstream, implying that the principal heat-release location advances toward the inlet, this is consistent with the upstream displacement of the high-temperature zone in Fig. 4.

To visualize the flame topology, the isosurface of$Y_{OH} = 0.005$ was extracted to identify flame. As shown in Fig. 5**c**, this isosurface overlaps well with the high-temperature zone in Fig. 4**c**, confirming OH as a reliable indicator of heat release. As the inlet velocity increases, the flame in SMC elongates and drifts toward the outlet, and becomes asymmetric at 7 m/s, then blow-off occurs at 8 m/s. In contrast, the TMC shows no tributary flame at 3 m/s, combustion occurs only in main channel, but at 5 and 7 m/s the main channel flame is shorter than in the SMC, and symmetric side flames form in the two tributary channels, yielding a “trident-shaped” flame morphology. This flame morphology, effectively embedded within the Tesla-valve, suppresses downstream flame recession and detachment, providing stronger anchoring. Consequently, compared with the conventional SMC, the Tesla-valve induced flame topology is pivotal to efficient combustion and flame stability at moderate–high inlet velocities.

To elucidate how the Tesla-valve structure regulates the flame, the flow characteristics of a straight micro combustor (SMC) and a Tesla-valve micro combustor (TMC) were systematically compared (Fig. 6). As shown in Fig. 6**a**, over an inlet-velocity range of 1–7 m/s, the pressure drop increases with velocity for both SMC and TMC, but the TMC remains a lower pressure loss. At 7 m/s, the drops are 532.48 Pa (SMC) and 440.64 Pa (TMC), showing a 17.25% reduction, and the disparity widens as velocity increases. Fig. 6**b** further clarifies the pressure drop behavior, the SMC develops a pronounced high-pressure zone at the

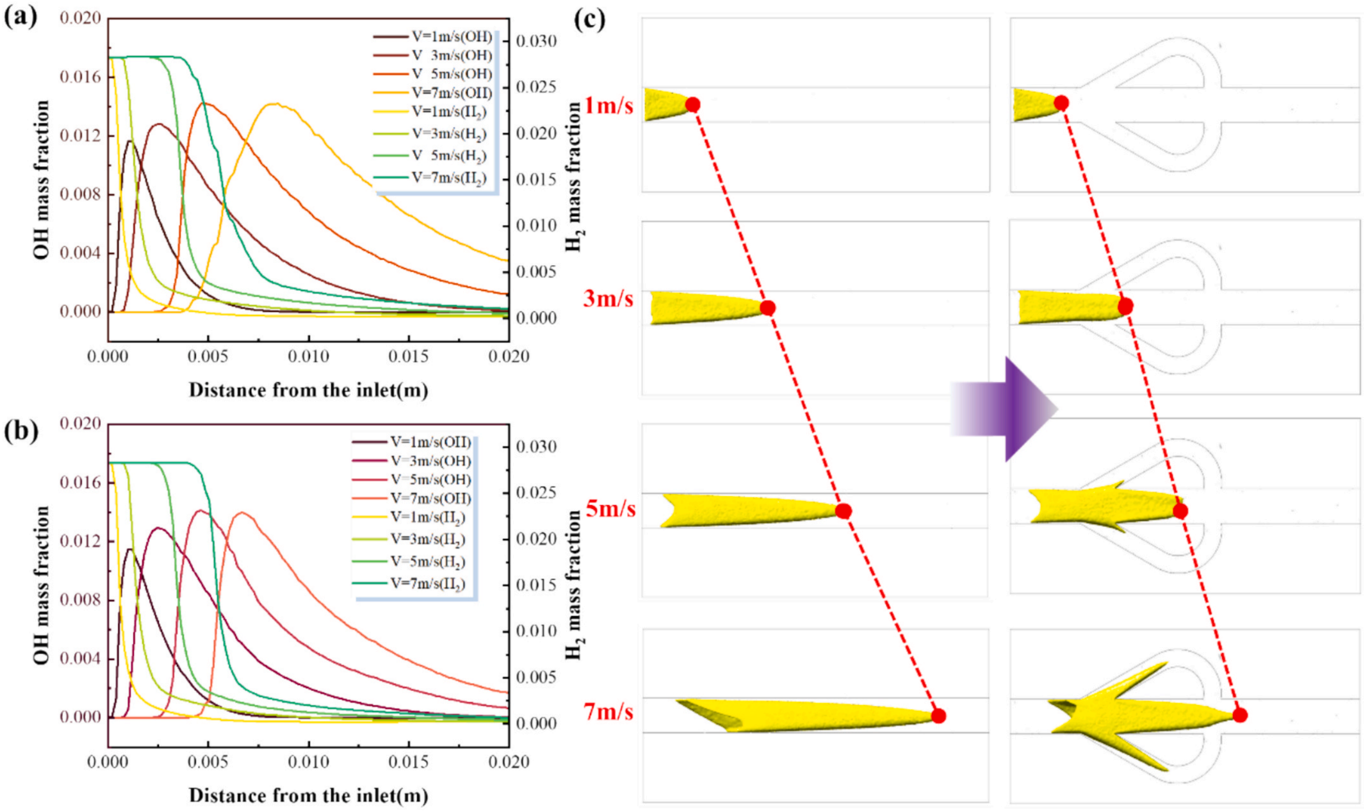

Fig. 5. Distributions of Y_{H_2} and Y_{OH} and flame topology. (a) Centerline Y_{H_2} and Y_{OH} in the SMC; (b) Centerline Y_{H_2} and Y_{OH} in the TMC; (c) Isosurfaces of $Y_{OH} = 0.005$ at 1, 3, 5, and 7 m/s (SMC: left; TMC: right). Red markers and dashed guides indicate the evolution of peak/anchor positions.

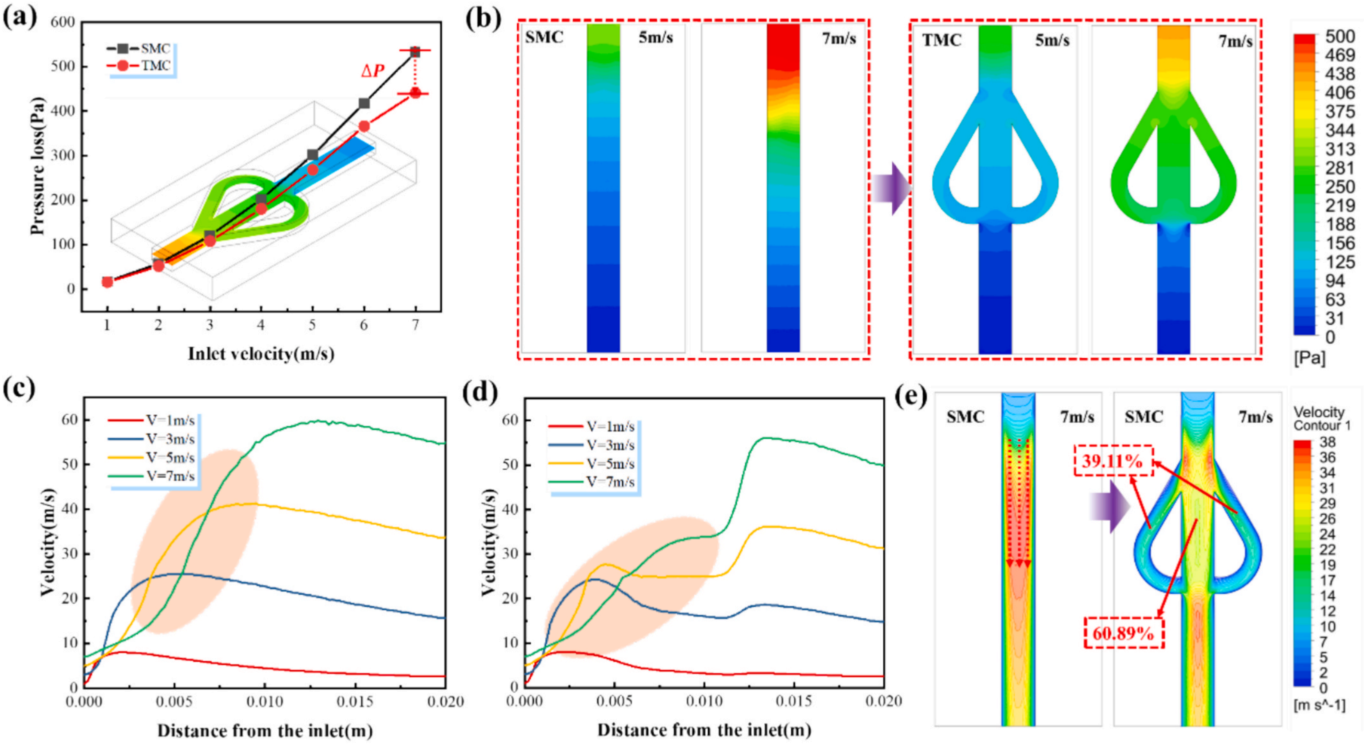

Fig. 6. Comparison of flow features between SMC and TMC. (a) Pressure drop versus inlet velocity (1–7 m/s) (b) Pressure contour between SMC and TMC (c) Centerline velocity versus in SMC versus inlet velocity (1–7 m/s) (d) Main channel centerline velocity in TMC versus inlet velocity (1–7 m/s) (e) Velocity contours of the SMC and TMC at 7 m/s, with the mass-flow-rate partitioning between the main channel and tributary channels in the TMC.

inlet followed by a steep downstream decay, whereas the TMC shows a markedly reduced inlet pressure and a more uniform distribution across the Tesla-valve channel for both the main and tributary channels. This low inlet-pressure with quasi-uniform valve pressure pattern results from effective sudden expansion and flow redistribution induced by the tributary channels, the locally enlarged effective area mitigates inlet acceleration and localized losses, while the confluence of main and tributary channels impose lateral damping and broadens the shear layer, thereby reducing the overall pressure drop, this is consistent with prior designs that introduce a sudden-expansion at inlets [40]. Consistently, according to Fig. 6**c–d**, the centerline-velocity distribution shows that the SMC maintains higher velocities and larger gradients in the upstream/middle channels, limiting residence time and pushing the reaction zone downstream. In contrast, the TMC develops a stable low-velocity zone within the valve zone, increasing local residence time and favoring an upstream-shifted reaction zone. Although the velocity becomes higher further downstream in the TMC, this region is mainly occupied by combustion products and has limited influence on upstream flame anchoring (Fig. 6**e**). To further quantify the flow redistribution induced by the Tesla-valve structure, the mass-flow-rate partitioning at 7 m/s was calculated. The results show that 60.89% of the total mass flow passes through the main channel, while 39.11% is diverted into the two tributary channels. This confirms that a considerable fraction of the incoming mixture participates in the tributary channel flow, providing lateral momentum interaction at the confluence and contributing to the blocking effect. Overall, within the low-to-moderate inlet-velocity range, the TMC relies on flow diversion and confluence to construct a low-velocity anchoring zone, reduce pressure loss, and suppress flame tilting, thereby enabling stable flame anchoring and higher combustion efficiency.

3.2. *Effect of inlet velocities*

Although the Tesla-valve micro-combustor (TMC) exhibits excellent flame anchoring and high efficiency at low inlet velocities, its behavior over a wider operating range requires systematic assessment. Accordingly, as shown in Fig. 7, reactive simulations were performed up to$u_{in} \le 42$ m/s. Based on the combustion efficiency η in Fig. 7**a**, three stages are identified: Stage I (2–22 m/s), a stable stage with$\eta > 90\%$, stage II (22–24 m/s), a switching transition of the Tesla-valve where η abruptly drops to 30.16%, and Stage III (24–40 m/s), a wall-attached partial re-stabilization stage under the present inert-wall assumption, in which η stabilizes at approximately 55%. This stable switching re-stabilized sequence correlates closely with the reaction zone evolution in the main channel and tributary channels. The centerline temperature in Fig. 7**b** confirms this phenomenon, as velocity increases, the main channel high-temperature zone gradually shifts downstream, reaching the outlet at$u_{in} = 22$ m/s, and for$u_{in} \ge 24$ m/s the high-temperature zone detaches from the main channel, consistent with the efficiency collapse in Stage II. As shown in Fig. 7**c**, the temperature contours further resolve the high-temperature zone distribution of each stage. In 2–22 m/s, a “neck-shaped” upstream high-temperature zone persists in the main channel while robust high-temperature zones remain in the tributary channels, providing thermal feedback for stable combustion. However, at 22 m/s the neck-shaped flame disappears, and for$u_{in} \ge 24$ m/s the main channel high-temperature zone leaves the combustor and two narrow wall-attached high-temperature zones emerge downstream, accompanying the partial efficiency recovery observed in Stage III. Overall, the TMC is different from conventional straight-channel micro combustors, especially the nonlinear variation feature between

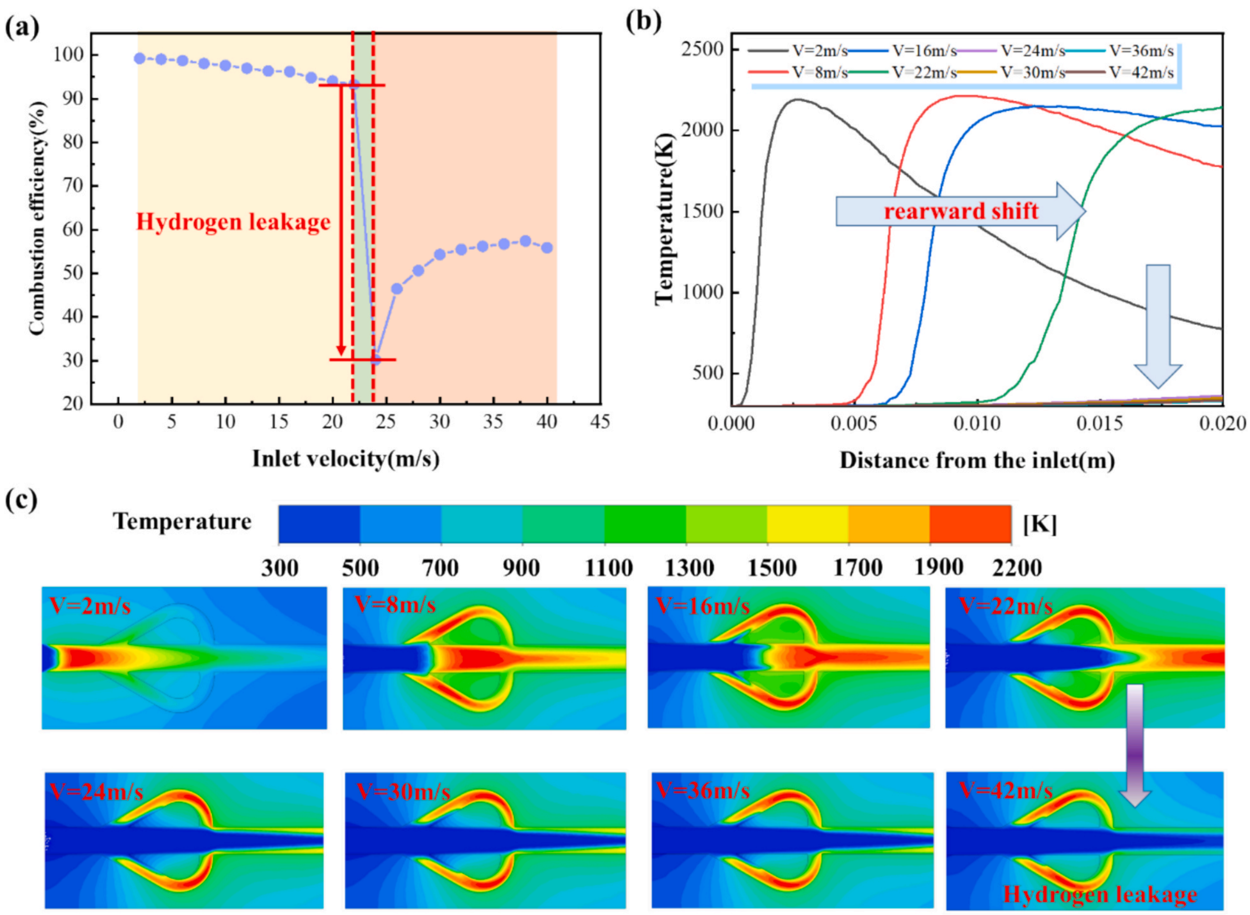

Fig. 7. Combustion and temperature characteristics of the Tesla-valve micro combustor over a wide inlet-velocity range ($u_{in} = 2$–42 m/s). (a) Combustion efficiency versus inlet velocity. (b) Centerline temperature profiles along the inlet. (c) Temperature contours at$u_{in} = 2$, 8, 16, 22, 24, 30, 36, and 42 m/s.

combustion efficiency and inlet velocity, which results in combustion diversity within a large inlet velocity range.

Fig. 8 presents the flame structure at different inlet velocities. As shown in Fig. 8**a**, the OH-radical isosurface is employed as a marker of the reaction zone and reproduces the high-temperature zone observed in Fig. 7**c**, confirming that the flame structure is consistent with the temperature field. Within 8–22 m/s, the side tributary flame affects the main channel flame, tributary channel inflows provide lateral damping in the valve and confluence zone, suppressing lift-off and enabling effective anchoring. As the velocity increases, the tributary channel momentum becomes insufficient to block the main channel gas, the flame progressively lifts, at 24 m/s, a clear detachment occurs, consistent with the rearward shift reported in Fig. 7. Besides, the combustion strength and stability are quantified by flame length (Fig. 8**b**), distinguishing the main channel flame length (*MFL*) from the tributary flame length (*TFL*), the latter defined as the projection of the branch flame along the main channel direction. Both lengths peak at 12 m/s, the $MFL = 0.015$ m and $TFL = 0.0075$ m are obtained, indicating optimal anchoring and coupling. Beyond 22 m/s the *MFL* nearly vanishes, whereas the *TFL* remains at 0.0028 m, implying that the tributary channels still supply thermal feedback for partial combustion. As shown in Fig. 8**c**, the OH mass-fraction profiles across the outlet further substantiate the spatial migration: at 8 m/s virtually no OH is detected at the exit, where flame residing inside the combustor. However, at 22 m/s a pronounced OH peak emerges at the exit (rearward shift), at higher velocities the centerline OH disappears while two off-axis peaks develop near the walls, forming a characteristic "flame opening" pattern. This bimodal OH distribution indicates wall-attached combustion with centerline fuel leakage, accounting for the reduced efficiency and energy loss, in agreement with the hydrogen leakage highlighted in Fig. 7. Therefore, future work should optimize the Tesla-valve geometry to deliver high-efficiency combustion over a broad operating range with robust flame stability, particularly suppressing "flame opening.".

To clarify how the Tesla-valve structure affects the gas distribution, the flow characteristics in the Tesla-valve combustor were further analyzed, as shown in Fig. 9. The pressure loss in Fig. 9**a** also exhibits three stages, consistent with the previously reported efficiency trend. Firstly, the pressure increases monotonically with inlet velocity in the range of 2–22 m/s. Then, it drops abruptly from 3,233.24 Pa to 1,160.92 Pa in 22–24 m/s, and then increases again monotonically at higher velocities. The two monotonic rises can be attributed to the increase in dynamic pressure with inlet velocity, whereas the sudden drop is associated with flow redistribution between the main and tributary channels. Accordingly, pressure contours at 22 m/s and 24 m/s were extracted (Fig. 9**b**). At 22 m/s, a distinct interface between high-pressure and low-pressure zones appears at the confluence, with high pressure mainly upstream in both the main channel and the tributary channels. At 24 m/s, although this division remains, the upstream pressure in both channels is significantly reduced. To clarify the cause, velocity fields were examined (Fig. 9**c**). At 22 m/s, the tributary channels exhibit high inlet velocity, indicating that a large portion of the gas is guided into tributary channels. At the confluence position, the tributary channel gas blocks the main channel gas from both sides and generates a high-velocity zone, which explains the higher pressure. In contrast, at 24 m/s the tributary channel gas is weakened and lower than the main channel gas velocity, the main channel gas dominates, lateral blockage is greatly reduced, and the pressure in both channels decreases. The streamline distributions in Fig. 9**d** reveal a clear redistribution of flow between the main and tributary channels. At 22 m/s, dense streamlines are observed in the tributary channels, indicating that a substantial portion of the incoming mixture is diverted into the side branches and subsequently interacts with the main channel flow at the confluence.

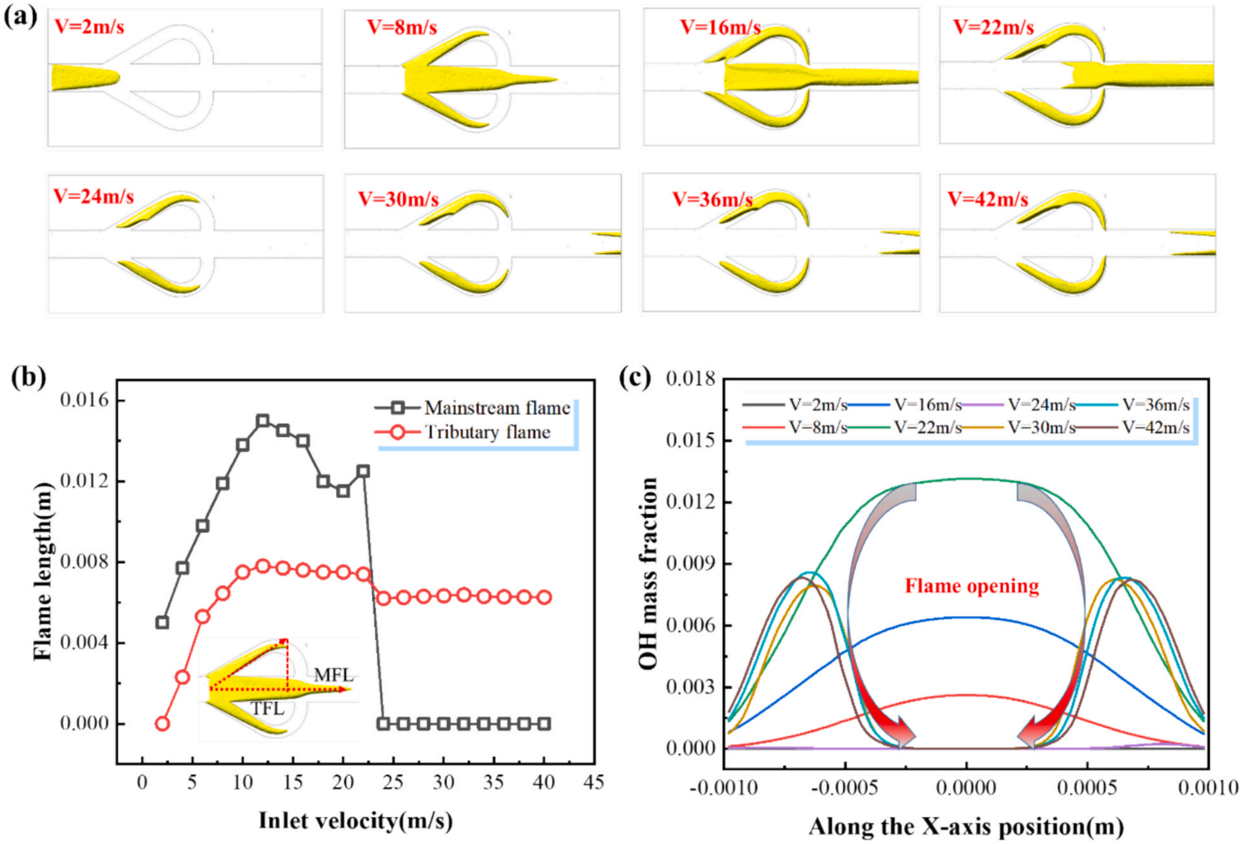

Fig. 8. Flame morphology of the Tesla-valve micro-combustor (TMC) at different inlet velocities. (a) 3D OH-isosurface flame shapes atu_{in} = 2, 8, 16, 22, 24, 30, 36, and 42 m/s. (b) Velocity dependence of flame length. (c) OH mass-fraction profiles along the outlet centerline.

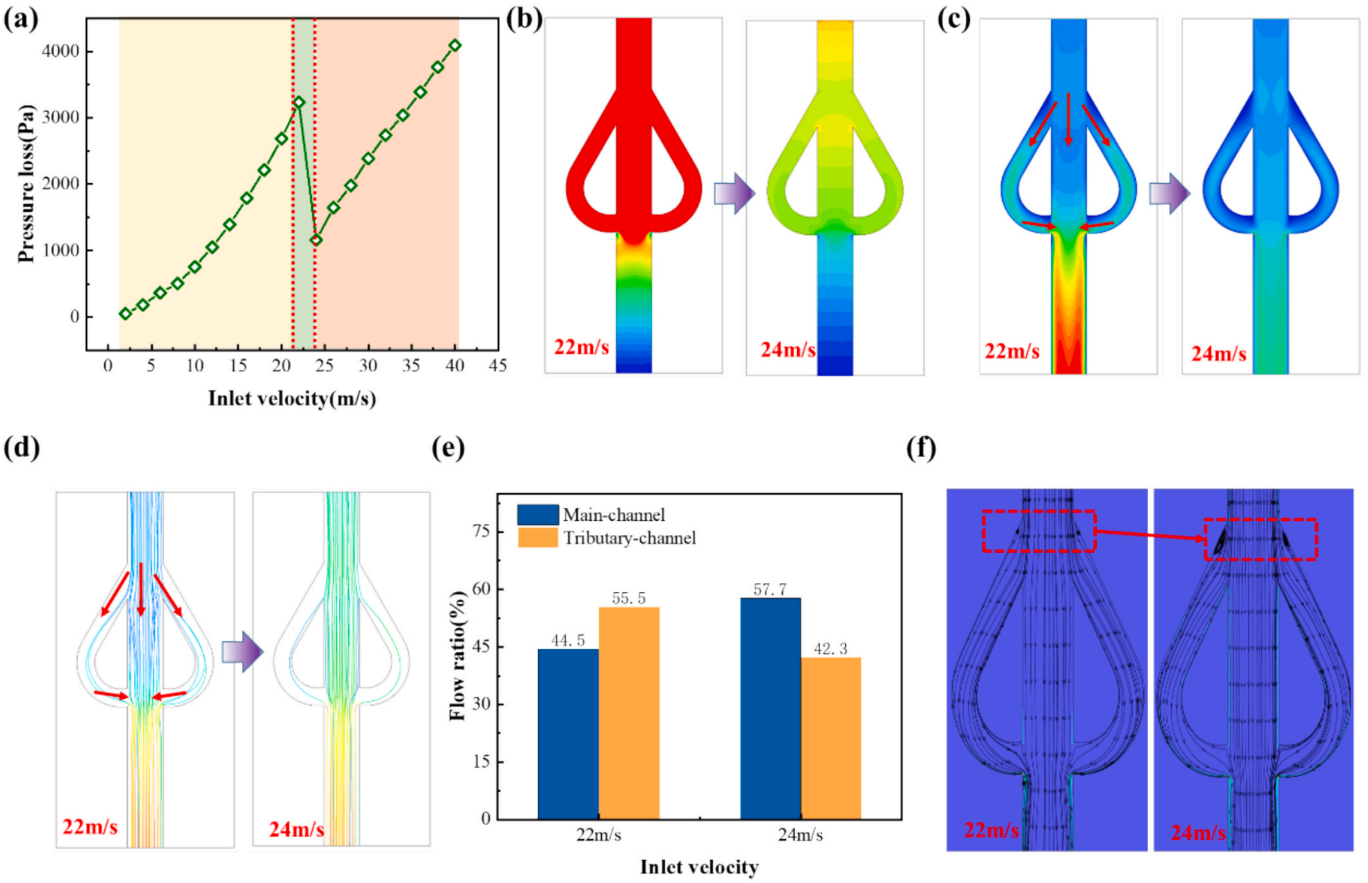

Fig. 9. Pressure evolution and flow mechanisms in the Tesla-valve micro-combustor (TMC). (a) Pressure drop versus inlet velocityu_{in} = 2–40 m/s. (b) Pressure contours at 22 and 24 m/s. (c) Velocity fields at 22 and 24 m/s. (d) Streamlines showing main channel and tributary channel flow paths. (e) The flow-rate partitioning across the main and tributary channels. (f) Vorticity and streamline distributions near the tributary channel entrances, showing local recirculation at 24 m/s without vortex shedding.

This interaction produces a pronounced lateral blocking effect. In contrast, at 24 m/s, most streamlines pass directly through the main channel, while the tributary channel streamlines are markedly reduced, indicating weakened branch-flow participation. The flow-rate partitioning was further quantified in Fig. 9**e**. As the inlet velocity increases from 22 to 24 m/s, the main channel flow ratio increases from 44.5% to 57.7%, whereas the tributary channel flow ratio decreases from 55.5% to 42.3%. This confirms a clear flow redistribution from tributary-assisted transport to main channel dominated penetration. The vorticity and streamline distributions in Fig. 9**f** further clarify the mechanism. No obvious vortex shedding is observed between 22 and 24 m/s. Instead, two local recirculation zones form near the tributary channel entrances at 24 m/s, which suppress gas admission into the tributary channels. Consequently, the tributary-induced blocking effect at the confluence is weakened, allowing the main channel flow to penetrate downstream more directly and leading to the abrupt reduction in pressure loss. Overall, the flow-rate balance between the main and tributary channels is crucial to combustion performance. Measures that enhance tributary flow participation and the associated blocking effect may strengthen flame anchoring.

3.3. *Effect of separation distance*

Building on the previous results, the flow diversion and confluence between the main channel and tributary channels are considered the primary reason for the observed switching behavior in combustion and flow characteristics. To further investigate this effect, Fig. 10**a** depicts two symmetric Tesla-valve islands forming the main channel and tributary channels, the separation distance d regulates the effective widths of both channels. Five separation distances were designed, d = 1.2, 1.6, 2.0, 2.4, and 2.8 mm, which are denoted as TMC-1.2, TMC-1.6, TMC-2.0, TMC-2.4, and TMC-2.8, respectively. This design keeps the total flow area nearly constant, so the changes in performance can be attributed mainly to flow diversion and confluence. Fig. 10**b** compares the combustion efficiency over 2–40 m/s for different separation distances. For TMC-1.2, the efficiency shows a slight, nearly linear decrease and still reaches 84.44% at 40 m/s. TMC-1.6 exhibits a milder switching behavior near 26 m/s, with 75.16% at 40 m/s, increasing d to 2.0 mm leads to a pronounced switching in TMC-2.0, followed by an increase that plateaus around 55%. A larger separation distance of d = 2.4 mm produces a severe drop, with the efficiency below 10% at 40 m/s and no clear rebound. With d = 2.8 mm, the switching is delayed to 30 m/s and the efficiency at high velocity recovers to above 50%. To relate these trends to the thermal performance, Fig. 10**c** presents the centerline temperature at 24 m/s. The high-temperature zone for TMC-2.4 and TMC-2.8 is generally more upstream, for TMC-1.2 and TMC-1.6, the high-temperature zone is close to the inlet but remains within the main channel, but for TMC-2.0, the high-temperature zone disappears, consistent with the switching seen in Fig. 10**b** at 24 m/s. The temperature contours in Fig. 10**d** further show that, as d increases, a high-temperature zone persists in the tributary channel but the area decreases, which is consistent with the reduced effective flow domain of the tributary channels. Meanwhile, the high-temperature zone in the main channel disappears from TMC-1.2 to TMC-2.0, indicating a rearward shift of the reaction zone, whereas wall-attached high-temperature zones re-forming for TMC-2.4 and TMC-2.8, which is consistent with the

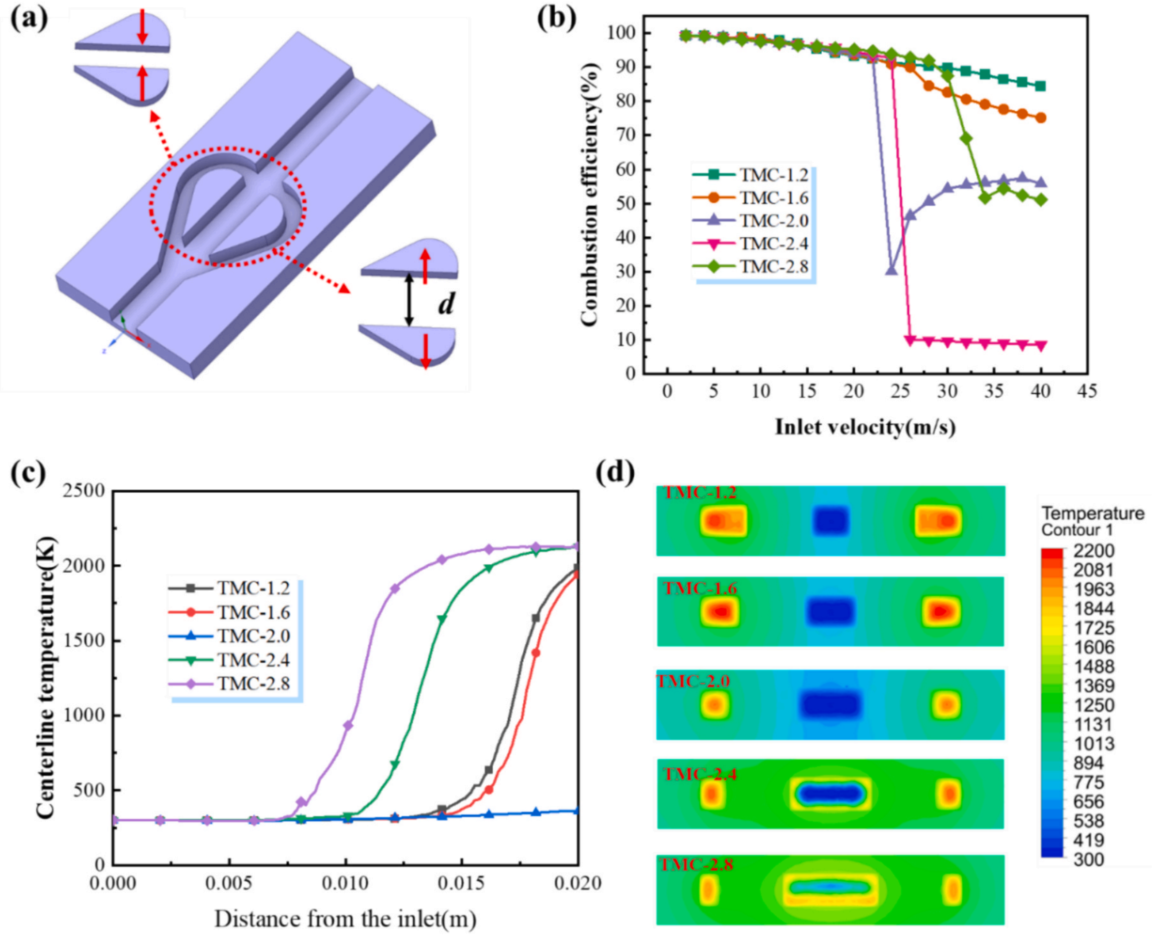

Fig. 10. Influence of the separation distance *d* on combustion efficiency and temperature fields. (a) Structure and definition of *d*, five separation distances *d* are considered: d = 1.2, 1.6, 2.0, 2.4, and 2.8 mm. (b) Combustion efficiency versus inlet velocity, u_{in}=2 − 42 m/s. (c) Centerline temperature along the main channel atu_{in} = 24 m/s. ((d) Temperature contours on the xy-plane at the slice z = − 0.01 m.

centerline temperature.

To assess the effect of *d* on the thermal performance, temperature contours were compared at three inlet velocities (14, 24, and 34 m/s) for different *d* values (Fig. 11). At an inlet velocity of 14 m/s, all combustors

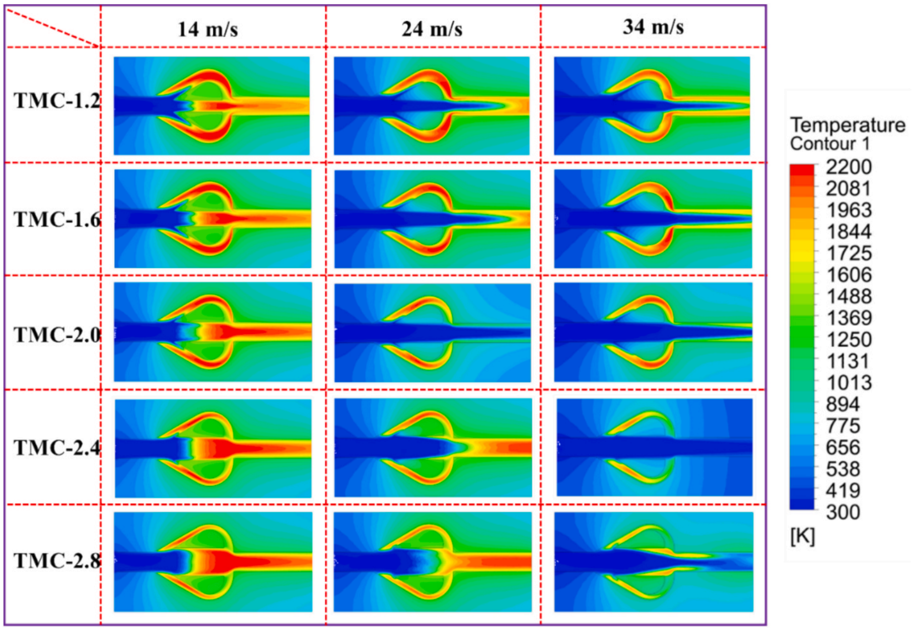

Fig. 11. Temperature contours for different Tesla-valve island separation distance (*d* = 1.2, 1.6, 2.0, 2.4, 2.8 mm) and inlet velocities(u_{in} =14, 24, 34 m/s).

exhibit a continuous high-temperature zone anchored near the valve/main channel, with stable high-temperature zones also visible in the tributary channels, the overall patterns are consistent across separation distance. Distinct differences emerge among separation distances at 14 m/s, in TMC-2.0, the high-temperature zone in the main channel is the first to weaken and become interrupted/lifted. Compared with TMC-1.2 and TMC-1.6, TMC-2.4 and TMC-2.8 show a more upstream location of the high-temperature zone, accompanied by a weakened high-temperature zone in the tributary channels. However, at a high inlet velocity of 34 m/s, smaller separation distances (TMC-1.2, TMC-1.6, TMC-2.0) still retain discernible downstream high-temperature zones. TMC-2.4 exhibits a pronounced detachment of the high-temperature zone with low temperatures dominating the channel, and TMC-2.8 shows a slight improvement relative to TMC-2.4, with a more continuous downstream high-temperature zone. Overall, at low inlet velocity (14 m/s), the temperature distribution is largely insensitive to separation distance. At mid-velocity (24 m/s), increasing separation distance weakens the main channel high-temperature zone, shifts it upstream, and reduces the tributary high-temperature zones. At high velocity (34 m/s), smaller separation distances better preserve downstream high-temperature zones, while among the larger separation distance TMC-2.8 displays a modest recovery compared with TMC-2.4.

As shown in Fig. 12, the OH isosurfaces are used to visualize flame morphology. At 14 m/s, all combustors exhibit a continuous “necked-shape” flame in the main channel that extends downstream as the island separation distance *d* increases, whereas the tributary channel flames progressively shorten and narrow with increasing *d*, consistent with the relative widening of the main channel flame. As inlet velocity increases to 24 m/s, the flames in TMC-1.2 and TMC-1.6 weaken and remain only weakly connected between the main and side tributary channels, and the main channel flame in TMC-2.0 is essentially lifted off. In contrast, for larger separation distances (d = 2.4 and 2.8 mm) the main channel flame shows stronger anchoring and continuity, which is consistent with attachment conditions provided by the main channel sudden-expansion–contraction structure. However, with an inlet velocity of 34 m/s, TMC-1.2 and TMC-1.6 display only a slight rearward shift while retaining identifiable structures, TMC-2.0 and TMC-2.4 exhibit further lift-off of the main channel flame accompanied by weakened tributary channel flames, despite a weaker tributary contribution, TMC-2.8 shows a downstream recovery into more continuous zones in the main channel, collectively indicating that, at higher velocities, larger *d* can be favorable to flame anchoring through the local main channel structure.

To quantify flame intensity across configurations, the main channel flame length (*MFL*) and tributary flame length (*TFL*) were measured (Fig. 8**b**) and combined as the effective flame length $EFL = MFL + TFL$. The resulting heat map in Fig. 13 uses color to represent *EFL* (red refer better combustion, blue refer weaker combustion), and distinct velocity windows are observed for different island separation distances. As shown in Fig. 13, the TMC-1.2 sustains large *EFL* over the entire velocity range (4–40 m/s), giving the broadest usable range, and TMC-1.6 likewise maintains high *EFL* with only a slight decay at the highest velocities. However, the TMC-2.0 exhibits strong *EFL* at low–mid velocities (4–22 m/s) followed by a rapid decline beyond 22–24 m/s. In addition, the TMC-2.4 narrows the effective range further to 4–26 m/s with a marked reduction above this limit, and TMC-2.8 preserves large *EFL* mainly in the mid-velocity band (8–30 m/s) before weakening at higher velocities. Overall, the *EFL* heat map is consistent with the earlier efficiency/temperature observations, with smaller separation distances (1.2–1.6 mm) provide the widest high-intensity combustion window, whereas larger separation distances (2.0–2.8 mm) show progressively lower upper-velocity limits. This *EFL*-based comparison provides geometry-specific insight into the effect of separation distance on flame-intensity windows, smaller separations distance for broader high-velocity operation, and larger separations distances for mid-velocity applications where the desired flame morphology can still be maintained.

Fig. 14 provides a quantitative comparison of OH and H_2 distribution for different separation distances (TMC-1.2 to TMC-2.8) at three inlet velocities. At 14 m/s, the OH distribution in the main channel widens with increasing *d*, whereas the OH at the side tributary channel locations narrows and weakens, indicating a lateral trade-off between the main and tributary flames (Fig. 14**a**). At 24 m/s, the OH distribution in the

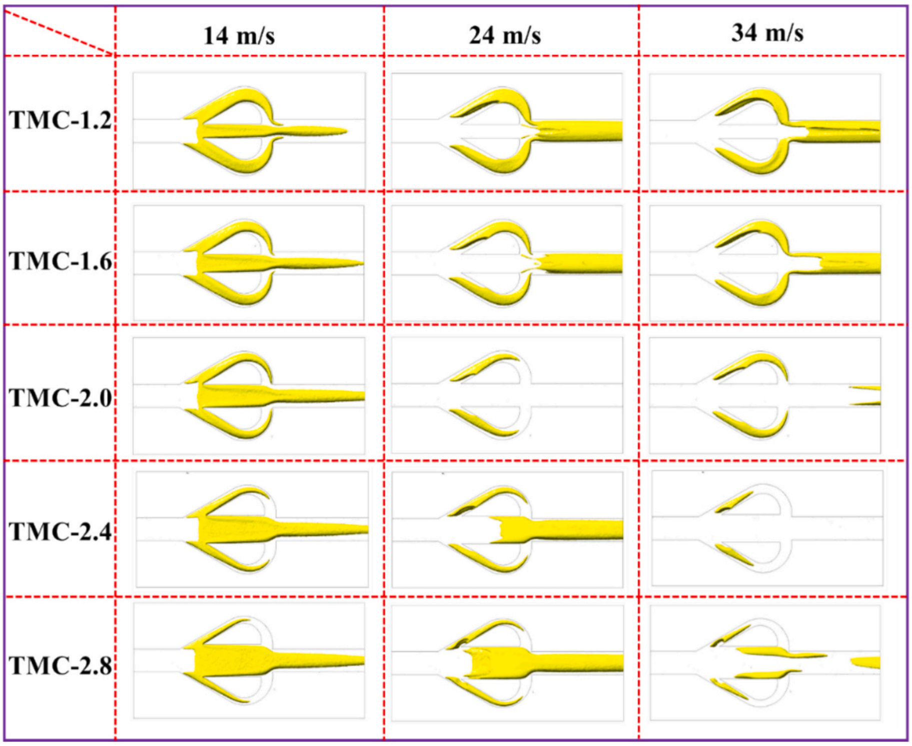

Fig. 12. OH mass fraction isosurface for different Tesla-valve island separation distance (d = 1.2, 1.6, 2.0, 2.4, 2.8 mm) and inlet velocities(u_{in} =14, 24, 34 m/s).

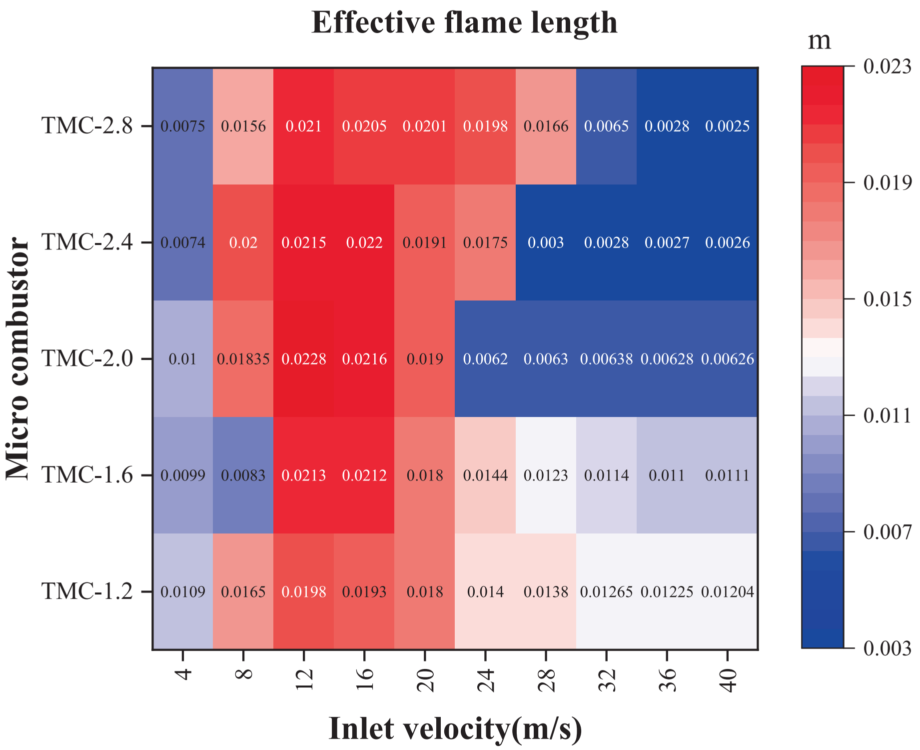

Fig. 13. Heat maps of effective flame lengths at different separation distances.

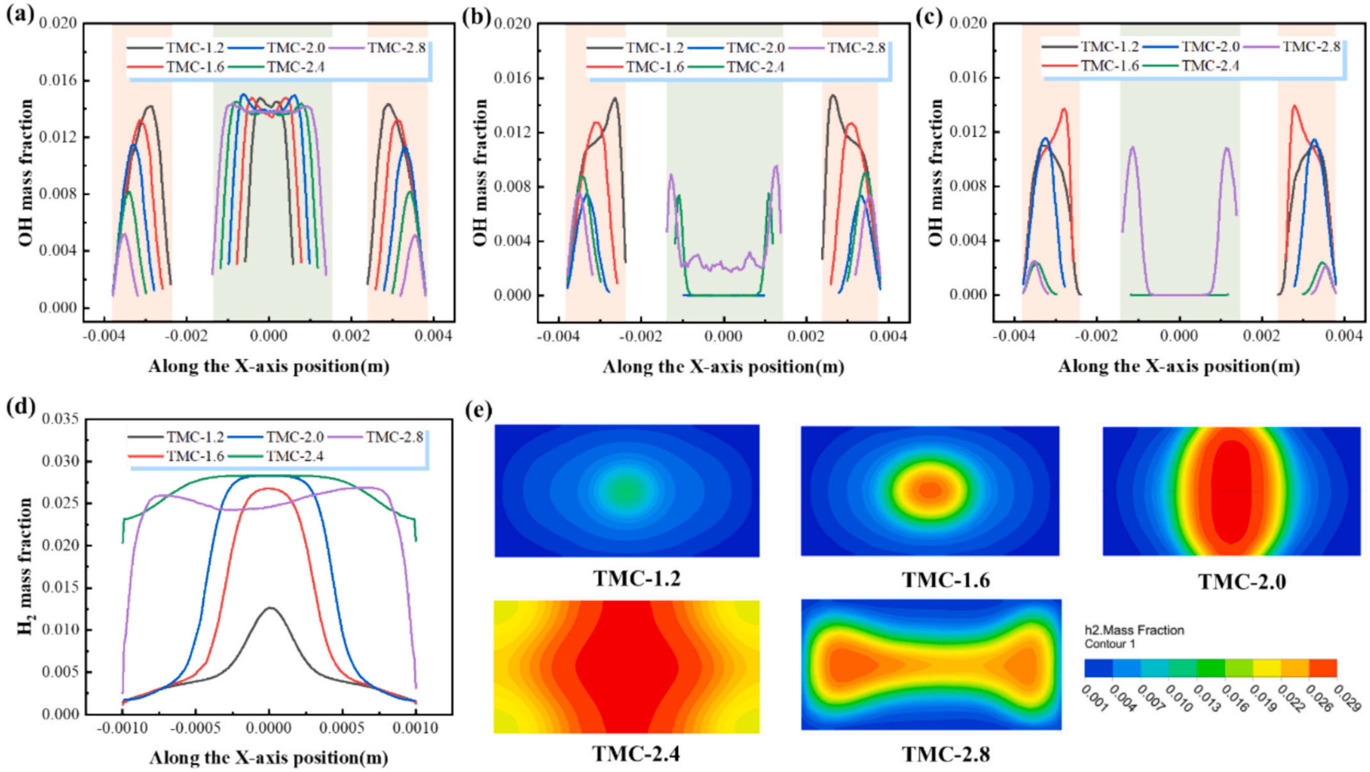

Fig. 14. Effect of Tesla-valve island separation distance *d* on reaction intensity and hydrogen leakage. (a–c) OH mass-fraction along the x-axis (z = − 0.01 m). (d) Centerline H_2 mass-fraction at Outlet (u_{in} = 34 m/s). (e) H_2 mass fraction contour on the outlet plane(u_{in} = 34 m/s).

main channel is attenuated to nearly absent, with flame concentrated at the two side positions, the smaller separation distances (TMC-1.2 and TMC-1.6) show higher OH mass fraction (Fig. 14**b**). At 34 m/s, the side tributary channel OH peaks decrease as *d* increases, where most evident for TMC-2.4 and TMC-2.8, but wall-attached OH zones emerge along the main channel, especially strongest for TMC-2.8, reflecting a shift of the combustion zone toward the walls and downstream (Fig. 14**c**). Consistently, as shown in Fig. 14**d-e**, the outlet H_2 mass fraction increases with velocity. At an inlet velocity of 34 m/s, the outlet H_2 mass fraction rises and concentrates near the centerline as d increases from 1.2 to 2.0 mm, and the outlet H_2 contours reveal an expanded high-hydrogen zone. For larger separation distances, especially in TMC-2.4 and TMC-2.8, the high-hydrogen zones become more intense and widespread, with TMC-2.4 exhibiting the largest extent and magnitude, indicating more pronounced fuel leakage at high inlet velocity. Overall, enlarging separation distance at mid-to-high velocities re-forms combustion from the main channel. At the same time, large separation distances will cause more serious hydrogen leakage, which is not conducive to the realization of complete combustion and flame stability, this result is consistent with the temperature-field and effective flame length variation.

To clarify the effect of separation distance d on combustion and flame behavior, pressure loss and velocity fields were analyzed to characterize the main/tributary flow interaction (Fig. 15). In Fig. 15**a**, TMC-1.2/1.6 shows a monotonic increase of pressure drop with inlet velocity, indicating strong lateral momentum exchange and local losses, leading sufficient branch suction that imposes pronounced lateral blocking on the main channel gas. TMC-2.0/2.4 exhibit a sudden drop at 22–24 m/s followed by increase, indicating a transition toward a main channel dominated state, in which the tributary channel momentum can no longer effectively constrain the main channel jet, thereby reducing local losses. TMC-2.8 has moderate pressure loss without a sharp drop, implying main channel flow dominance but geometry-assisted attachment via the sudden expansion contraction, favorable for downstream re-anchoring. As shown in Fig. 15**b**, cross-sectional velocity confirms that increasing d weakens the tributary high-velocity zones and strengthens the main flow zone, consistent with pressure loss trends and indicating erosion of the low-velocity zone in Tesla-valve channel. The velocity and vector fields in Fig. 15**c** further show that at 14 m/s all cases develop a low-velocity zone, within, smaller separation distance, the TMC-1.2 and TMC-1.6 provide stronger side injection, thicker shear, and robust mixing, supporting a neck-shaped attached flame, whereas larger separation distance, TMC-2.4 and TMC-2.8 yields a straighter, thinner main jet with a reduced zone. At 24 m/s, the TMC-2.0 and TMC-2.4 lose lateral blocking, the main channel jet punches through, residence time shortens, and the flame shifts downstream or breaks up, while TMC-1.2 and TMC-1.6 still maintain attachment. At 34 m/s, the main channel dominates, small separation distance retains narrow wall-attached zones downstream, TMC-2.0 and TMC-2.4 are most prone to opening and hydrogen leakage, and TMC-2.8 benefits from structure-induced wall attachment and weak recirculation for re-anchoring, outperforming TMC-2.4. For the present geometry, the separation distance should be selected based on a multi-objective trade-off among combustion efficiency, flame stability, and pressure-drop penalty. Smaller separations, such as $d = 2.0$–2.4 mm, favor broad-range flame stabilization but introduce higher pressure loss, whereas $d = 2.8$ mm may be more suitable for high-velocity or pressure-constrained operation by enabling downstream wall-attached re-stabilization with a relatively moderate pressure penalty. In addition, additional factors may influence the switching behavior and flame morphology in Tesla-valve micro channels, particularly the tributary geometry (length and radius) and the

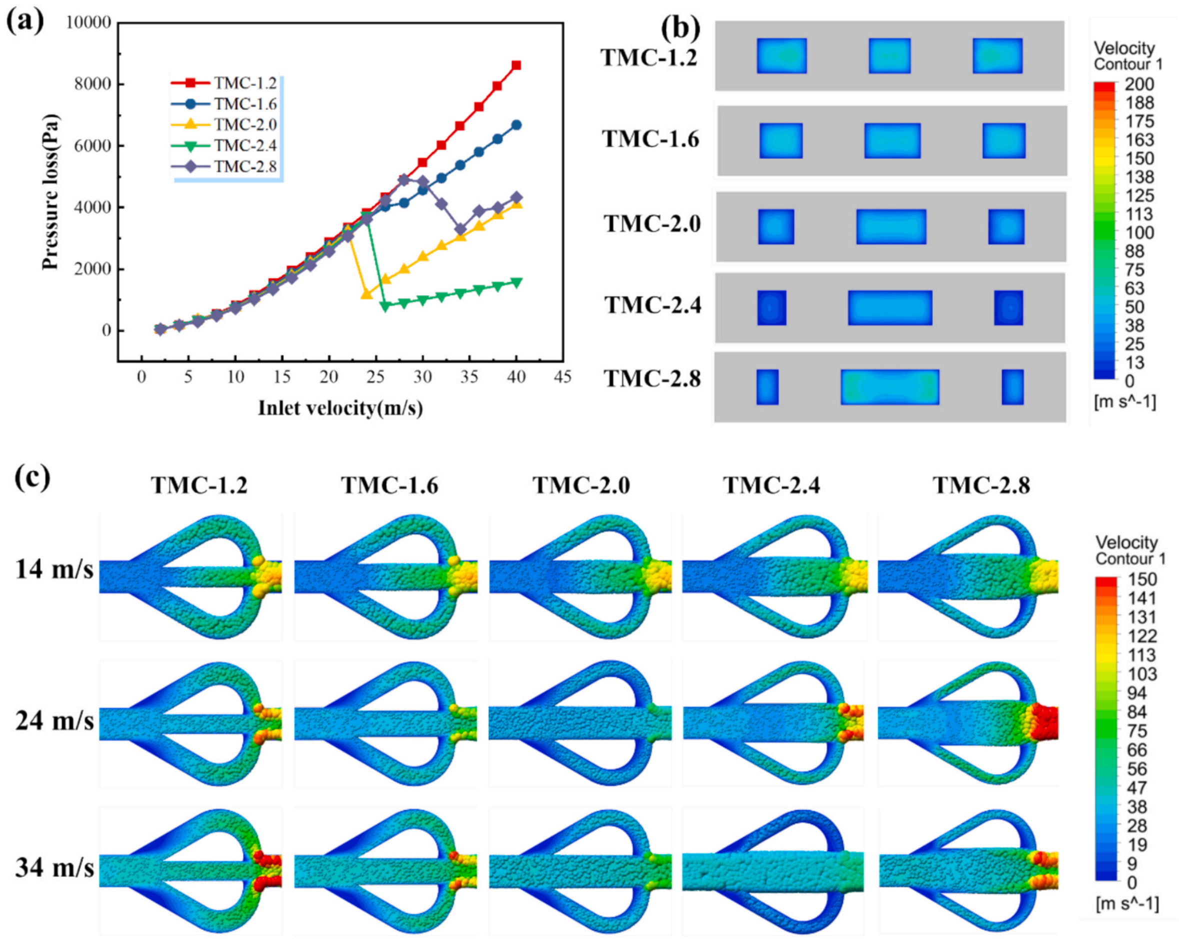

Fig. 15. Influence of Tesla-valve island separation distance on the flow characteristics in micro-combustor. (a) Pressure drop versus inlet velocity for five separation distances (TMC-1.2, TMC-1.6, TMC-2.0, TMC-2.4, TMC-2.8). (b) Velocity-magnitude contours at xz-plane within the valve section, highlighting high/low-velocity zones of the main and tributary channels (y = 0.0005 m). (c) Velocity fields (magnitude and vectors) at$u_{in} = 14, 24, 34$ m/s, columns correspond to the five separation distances and rows to the three operating velocities.

diversion/convergence angles between the main and tributary channels, and these effects will be reported in future work.

4. Conclusion

This work proposes and systematically investigates a symmetric Tesla-valve micro-combustor (TMC), elucidating its impact on combustion efficiency and flame morphology. In the low-velocity regime (1–7 m/s), the TMC outperforms a straight micro-combustor (SMC), achieving a peak combustion efficiency of 98.09% while reducing the pressure drop by 17.25%. This improvement is attributed to tributary-induced lateral blocking in the valve section, which forms a distinctive trident-like anchored flame.

Across a wide inlet-velocity range (2–40 m/s), a pronounced switching transition occurs at 22–24 m/s, where combustion efficiency drops from 93.23% to 30.16% and the pressure drop decreases from 3,233.24 Pa to 1,160.92 Pa. This transition coincides with detachment of the main channel flame, flame opening, and fuel leakage, confirming the strong velocity dependence of main/tributary flow partitioning. Building on this observation, the influence of Tesla-valve island separation distance is further examined. Small separations ($d = 1.2$ and 1.6 mm) strengthen tributary blocking and thicken the lateral shear layer, enhancing flame anchoring and efficiency at the cost of increased pressure loss. Intermediate separations ($d = 2.0$ and 2.4 mm) weaken blocking, allowing main channel penetration that triggers switching behavior and induces flame opening or lift-off. In contrast, a larger separation ($d = 2.8$ mm) promotes mild low-velocity recirculation via sudden expansion–contraction, stabilizing a wall-attached flame and partially recovering efficiency at high velocities.

Therefore, the separation distance should be determined through a balanced consideration of combustion efficiency, flame stability, and pressure-drop penalty. For the present TMC geometry, small separations are preferred when broad-range flame stabilization and high combustion efficiency are prioritized, although they require a higher pressure-loss cost. For high-velocity or pressure-drop-constrained operation, a larger separation is more appropriate because it reduces excessive flow resistance while still enabling downstream wall-attached flame stabilization.

Although this study preliminarily reveals the effects of the Tesla-valve structure on flow organization, flame morphology, and combustion stability in microscale combustion, some limitations remain. The Tesla-valve micro-combustor contains multiple coupled geometric parameters, while their interactions and structural optimization have not been systematically investigated in this work. Future studies will combine theoretical analysis with multi-objective optimization to clarify the influence of key geometric parameters on combustion performance and identify an optimized micro-combustor design with high flame stability, low flow resistance, and favorable thermal management capability.

CRediT authorship contribution statement

Chenghua Zhang: Writing – original draft, Software, Investigation, Funding acquisition, Conceptualization. **Yunfei Yan:** Formal analysis, Conceptualization. **Yonghong Wu:** Software, Formal analysis, Data curation. **Zikang Niu:** Visualization, Investigation, Data curation. **Chang Liu:** Formal analysis, Data curation. **Wen Siang Lew:** Writing – review & editing, Formal analysis.

Declaration of competing interest

The authors declare that they have no known competing financial interests or personal relationships that could have appeared to influence the work reported in this paper.

Acknowledgments

This research was supported by the Doctoral Program of National Natural Science Foundation of China (525B2095), the General Program of the National Natural Science Foundation of China (52576106) and the China Scholarship Council (Grant No. 202506050076).

Data availability

No data was used for the research described in the article.

References

[1] Mei JEY, Feng C, Ding J, Cai L, Luo B. A review of enhancing micro combustion to improve energy conversion performance in micro power system. Int J Hydrogen Energy 2022;47(53):22574–601.

[2] Wan J, Fan A. Recent progress in flame stabilization technologies for combustion-based micro energy and power systems. Fuel 2021;286:119391.

[3] Ding JEJ, Chen J, Liao G, Zhang F, Luo B. Process in micro-combustion and energy conversion of micro power system: a review. Energ Conver Manage 2021;246:114664.

[4] Li J, Li Y. Micro gas turbine: Developments, applications, and key technologies on components. Propul Power Res 2023;12(1):1–43.

[5] Cai T, Tang A, Zhang Q, Ni Q, Li J. A systematic review of enhancing stabilization performance and mitigating thermoacoustic instability in renewable ammonia turbulent combustion. Renew Sustain Energy Rev 2025;217:115760.

[6] Ni S, Zhao D. NOx emission reduction in ammonia-powered micro-combustors by partially inserting porous medium under fuel-rich condition. Chem Eng J 2022;434:134680.

[7] Rong H, Zhao D, Becker S, Liu X. Entropy production and thermodynamics exergy investigation on an ammonia-methane fueled micro-combustor with porous medium for thermophotovoltaic applications. Int J Hydrogen Energy 2024;49:384–400.

[8] Lu Q, Zhou H, Zhang Y, Gou J, Fan B, Jiang C, et al. Experimental and numerical investigations on hetero-/homogeneous combustion characteristics of C_3H_8/Air mixtures in the micro catalytic combustor. Appl Therm Eng 2025;274:126638.

[9] Nauman M, Pan J, Lu Q, Zhang Y, Liu C, Li F, et al. Analyzing the combustion characteristics of premixed methane-oxygen with different hydrogen addition ratios in a catalytic micro-combustor. J Energy Inst 2024;114:101655.

[10] Lin E, Wilson CT, Leroy A, El Fil B. High energy density entrainment-based catalytic micro-combustor for portable devices. Energ Conver Manage 2023;285:117014.

[11] Lv E, Liu W, Zhang G, Fan A. Analysis of entropy generation and exergy efficiency of a micro-combustor with a passive exhaust gas recirculation channel. Int J Hydrogen Energy 2024;86:1337–47.

[12] Wu Y, Yan Y, He Z, Zhang C, You J, Xue Z. A novel micro-combustor with dual-inlets hedging and center opening for enhancing comprehensive performance of micro thermophotovoltaic system. Appl Therm Eng 2024;252:123564.

[13] Xu B, Liu W, Fan A. Numerical investigation on combustion performances of premixed H_2-air jet flames above a sudden expansion micro-nozzle. Case Stud Therm Eng 2025;74:106979.

[14] Zuo W, Zhang Y, Li Q, Li J, He Z. Numerical investigations on hydrogen-fueled micro-cylindrical combustors with cavity for micro-thermophotovoltaic applications. Energy 2021;223:120098.

[15] Zuo W, Li D, Xia JEY, Li Q, Quan Y, Zhang G. Parametric study of cavity on the performance of a hydrogen-fueled micro planar combustor for thermophotovoltaic applications. Energy 2023;263:126028.

[16] Peng Q, Zhang JEZ, Hu W, Zhao X. Investigation on the effects of front-cavity on flame location and thermal performance of a cylindrical micro combustor. Appl Therm Eng 2018;130:541–51.

[17] Gao W, Yan Y, Huang L, Shen K, He Z, Gao B. Numerical comparison of premixed H_2/air combustion characteristic of three types of micro cavity-combustors with guide vanes, bluff body, guide vanes and bluff body respectively. Int J Hydrogen Energy 2021;46(47):24382–94.

[18] Lu Q, Wang Q, Fan B, Zhang Y, Wang Y, Nauman M, et al. Numerical study on hydrogen heterogeneous reaction characteristic in a micro catalytic combustor with blunt body. Fuel 2024;357:126028.

[19] Zhang C, Yan Y, Shen K, Xue Z, You J, He Z. Comparative analysis of combustion stability and flow performance in micro combustor based on the synergistic action of slotted blunt body and front-baffle. Appl Therm Eng 2024;237:121802.

[20] Zhang C, Yan Y, He Z, Xue Z, You J, Jin R, et al. Promoting energy efficient conversion: Synergic-improving combustion efficiency and flame stability via front baffle and slotted blunt body in a micro combustor. Renew Energy 2024;231:120995.

[21] Zhang C, Yan Y, Wu Y, Meng X, Hu Y, Liu C. Constructing slotted bluff body with adaptively-regulated rear baffles for stable dynamic combustion in micro-combustors. Energy 2025;337:138629.

[22] Xu J, Ding X, Hu Z, Lou Q. Research on the loop heat pipe (LHP) wicks with the structure of Tesla valve. Appl Therm Eng 2025;281:128724.

[23] Wei Z, Yulong Z, Yulong G, Kunyu C, Haojie C. Study on the start-up characteristics and thermal-dynamic performance of pulsating heat pipes with Tesla valve: a numerical case. Appl Therm Eng 2025;280:128525.

[24] Xiong M, Yang J, Ding X, Li H, Zhang H. Topology optimization design of micromixer based on principle of Tesla valve: an experimental and numerical study. Chem Eng Process-Process Intensif 2023;193:109560.

[25] Chen L, Su C, Li S, Ye K. Design and diodicity enhancement mechanism of a double-baffle Tesla valve. Int J Mech Sci 2025;302:110575.

[26] Hu H, Son I, Kikumoto H, Zhang B, Hayashi K. Improving Tesla valve shape within fluid diode plates for building ventilation. Build Environ 2024;252:111259.

[27] Huang F, Ren L, Xie S, Leng M, Liao P. Numerical study of flow characteristics and heat transfer mechanism in Tesla valve tube. Results Eng 2024;21:101795.

[28] Soltani A, Pourfallah M, Seyed Sabour SMJ. Thermal enhancement of PEM fuel cell cooling with novel configurations of Tesla valve and hybrid nanofluids: a numerical study. Int J Hydrogen Energy 2024;69:1263–75.

[29] Rong H, Zhao D. Thermodynamic and entropy generation analyzes of Telsa-valve structured meso-scale combustors fuelled with hydrogen for thermophotovoltaic applications. Energy 2024;307:132788.

[30] Zhao H, Zhao D, Wang B, Shi B. Electrical power, energy efficiency, and acoustic performance investigations of a hydrogen-fueled micro-thermal photovoltaic system with a tesla valve-shaped micro-combustor. Appl Therm Eng 2024;256:124127.

[31] Rong H, Zhao D. Performance analyzes on Telsa-valve structured meso-combustors in presence of ammonia-hydrogen/air combustion for thermophotovoltaic applications. Renew Energy 2025;243:122546.

[32] Shen Y, Liu X, Li B, Zhang C, Liu L, Li W. Study on flame quenching characteristics inside the Tesla valve structure flame arrester unit. J Loss Prev Process Ind 2024;90:105351.

[33] Wei Y, Yan Y, Zhang C, Wu Y, You J, He Z. Numerical study of combustion characteristics and flame evolution behavior in a micro-planar combustor under sudden changes in operating conditions. Renew Energy 2025;242:122421.

[34] Gao W, He Z, Qi W. Enhancing micro thermophotovoltaic system efficiency via a Gyroid lattice-embedded micro combustor: performance comparison and optimization. Energy 2025;330:136959.

[35] Kuo CH, Ronney PD. Numerical modeling of non-adiabatic heat-recirculating combustors. Proc Combust Inst 2007;31(2):3277–84.

[36] Wu Y, Yan Y, Zhang C, Xue Z, Li Y, Hu Y, et al. Enhancing outer wall temperature uniformity in a micro-combustor for micro thermophotovoltaic system via four-corner tangential inlets injection. Fuel 2025;401:135849.

[37] Li J, Zhao Z, Kazakov A, Dryer FL. An updated comprehensive kinetic model of hydrogen combustion. Int J Chem Kinet 2004;36(10):566–75.

[38] Yan Y, Wei Y, Wang D, You J, He Z, Zhang C. Numerical study on combustion and energy efficiency characteristics of thermophotovoltaic-thermoelectric two-stage utilization system filled with porous media. Energy 2024;308:132909.

[39] Tang A, Pan J, Yang W, Xu Y, Hou Z. Numerical study of premixed hydrogen/air combustion in a micro planar combustor with parallel separating plates. Journal of Hydrogen Energy 2015;40:2396–403.

[40] Hu L, Lei H, Yin R, Fu G, Yang X, Peng Q. Investigation on improved energy conversion and efficiency of zero-carbon fueled the combustor with stepped-inlet and multi-channel outlets for micro thermophotovoltaic application. Appl Therm Eng 2025;279:127942.